



CFD investigation of the atmospheric boundary layer under different thermal stability conditions



J.E. Pieterse*, T.M. Harms

Department of Mechanical and Mechatronic Engineering, Stellenbosch University, South Africa

ARTICLE INFO

Article history:

Received 18 February 2013

Received in revised form

25 July 2013

Accepted 26 July 2013

Available online 1 September 2013

Keywords:

Monin–Obukhov theory

Thermal stratifications

Adiabatic lapse rate

Cosine hill

Transverse dune

ABSTRACT

An accurate description of the atmospheric boundary layer (ABL) is a prerequisite for computational fluid dynamics (CFD) wind studies. This includes taking into account the thermal stability of the atmosphere, which can be stable, neutral or unstable, depending on the nature of the surface fluxes of momentum and heat. The surface fluxes and vertical profiles of wind velocity and temperature are described by Monin–Obukhov similarity theory. The implementation of this thermally stratified atmosphere into CFD has been examined in this study by using Reynolds-averaged Navier–Stokes (RANS) turbulence models, and the commercial code STAR-CCM+. The maintenance of the temperature, velocity and turbulence profiles along an extensive computational domain length was required, while simultaneously allowing for full variation in pressure and density through the ideal gas law. Effects of gravity and buoyancy were included, leading to the emergence of the hydrostatic pressure field and the resultant density changes expected in the real atmosphere. The CFD model was tested against measured data, from the literature, for the flow over a cosine hill in a wind tunnel. The standard $k-\epsilon$ and SST $k-\omega$ turbulence models represented the data most accurately. The flow over an idealised transverse dune immersed in the thermally stratified ABL was also investigated. It was found that the flow recovery was enhanced and re-attachment occurred earlier in unstable conditions, while flow recovery and re-attachment took longer in stable conditions. The effect of the dune on the flow higher up in the atmosphere was also felt at much higher distances for unstable conditions, through enhanced vertical velocities. Under stable conditions vertical velocities were reduced. This confirmed that the assumption of neutral conditions could lead to an incomplete picture of the flow conditions that influence any particular case of interest.

© 2013 Elsevier Ltd. All rights reserved.

1. Introduction

The greater part of human endeavour occurs on the surface of our planet, where the interaction of the surface and the atmosphere leads to the formation of the atmospheric boundary layer (ABL). A thorough understanding of the processes taking place in the ABL is of utmost concern to humans, and computational fluid dynamics (CFD) is increasingly being used to study a wide variety of processes in the ABL, where its accurate modelling is an imperative precondition (Blocken et al., 2007a; Hargreaves and Wright, 2007; Kim and Boysan, 1999; Yang et al., 2008). These numerical simulations can be performed by using either the Reynolds-averaged Navier–Stokes (RANS) equations or by conducting large-eddy simulations (LES). LES generally provides more accurate solutions for the flow field but are at least one order of magnitude more computationally expensive than RANS (Rodi, 1997). For this reason practical simulation of ABL flows often

employ RANS in combination with two-equation turbulence models (Parente et al., 2011a).

The specific structure of ABL turbulence is strongly influenced by the daily cycle of surface heating and cooling (Garratt, 1994). Strong radiative heating of the ground by the sun results in heat transfer to the air and the formation of the convective or unstable ABL, with buoyancy forces that tend to destabilise displaced air parcels. A stable ABL results when the ground cools, and heat is transferred from the air to the ground (usually under nocturnal conditions), with the formation of temperature inversions close to the surface (Garratt, 1994). Neutral conditions only result when there is no heat transfer between the air and the ground, and buoyancy effects are absent. The velocity and temperature profiles that characterise the atmosphere under these different stability conditions are best described by Monin–Obukhov similarity theory (Arya, 2001b). Some attempts have been made to simulate the ABL under these conditions using RANS two-equation turbulence models (Alinot and Masson, 2005; Huser et al., 1997; Meissner et al., 2009; Pontiggia et al., 2009). The minimum requirement of the turbulence model for thermally influenced ABL flows is that it should account for both shear and buoyancy produced turbulence.

The concepts of atmospheric stability are above all applicable to the natural environment found in desert ecosystems. This includes

* Correspondence to: University of Stellenbosch, Private Bag X1 Matieland 7602, South Africa. Tel.: +27 839830118.

E-mail addresses: cpeterse@innowind.com, pieterseje@gmail.com (J.E. Pieterse).

the dynamics that control the formation, erosion and migration of sand dunes. Up until now though, no one has investigated the effect of the thermally influenced atmospheric boundary layer on the flow over a sand dune (Livingstone et al., 2007). Parsons et al. (2004b) modelled the flow over an idealised transverse dune under neutral conditions and found a deceleration of the flow immediately upwind of the dune followed by windward slope acceleration to a maximum velocity at the crest and subsequent flow reversal and separation in the lee. These results corresponded well to previous investigations (Livingstone et al., 2007; Parsons et al., 2004a; Wiggs et al., 1996). A major advantage of CFD in the study of flow over dunes lies in resolving the flow in the separation zone on the lee side (Livingstone et al., 2007).

The purpose of this study is therefore the CFD simulation, using the commercial code STAR-CCM+, of the thermally stratified ABL while accounting for buoyancy effects through full variation in temperature, pressure and density. The standard $k-\varepsilon$ and SST $k-\omega$ turbulence models, modified for gravity effects, will be used to demonstrate this. Maintenance of the flow profiles along an extensive domain length must be demonstrated. The accuracy of different turbulence models in predicting separation will be tested against measured data, found in the literature, for flow over a cosine shaped hill. Furthermore the effect of atmospheric thermal stratification on the flow over a sand dune will be clarified.

2. Formulation

The numerical description of the flow is based on the Reynolds-averaged Navier–Stokes (RANS) equations for steady conditions where the rotational effects of the Earth i.e., Coriolis force can be ignored. The effect of thermal stratification leads to buoyancy effects that have to be captured by the CFD, along with other effects of gravity such as buoyant production of turbulence.

2.1. Governing equations

The continuity, momentum and energy equations must have the effects of gravity reflected in their formulation. Terms describing these effects are shown as additional source terms, which must be added to the governing equations in STAR-CCM+, and temperature gradients are reformulated to be based on the potential temperature θ (Arya, 2001b), which is related to temperature by

$$\frac{\partial \theta}{\partial z} = \frac{\theta}{T} \left(\frac{\partial T}{\partial z} + \Gamma \right) \cong \frac{\partial T}{\partial z} + \Gamma \quad (1)$$

Potential temperature has the property of being conserved with height. Potential temperature gradient with height under neutral conditions is zero, while it is positive under stable conditions and negative under unstable conditions. Here Γ is the dry adiabatic lapse rate and is described as

$$\Gamma = g/c_p \quad (2)$$

Here g is the gravitational acceleration (9.81 m/s^2) and c_p is the specific heat at constant pressure. The continuity, momentum and energy equations are

$$\int_A \rho u_i n_i dA = 0 \quad (3)$$

$$\int_A \rho u_j u_i n_i dA = - \int_A P \delta_{ij} n_i dA + \int_A \tau_{ij} n_i dA + \int_V S_m dV \quad (4)$$

$$\int_A \rho c_p T u_i n_i dA = \int_V S_m u_i dV + \int_A \left[u_j \tau_{ij} + \frac{c_p \mu_t}{\sigma_T} \left(\frac{\partial \theta}{\partial x_i} \right) \right] n_i dA \quad (5)$$

where A is the outer surface area of a fixed volume V , u_i is the velocity component along the x_i direction, n_i is the cosine director of the outward unit vector \mathbf{n} perpendicular to the control surface dA , δ_{ij} is the Kronecker delta, τ_{ij} is the viscous stress tensor which includes the Reynolds stress tensor, ρ is the density, and σ_T is the turbulent Prandtl number for energy (Alinot and Masson, 2005; Pontiggia et al., 2009). Also, S_m is the momentum vector source term that adds the force of gravity to the volume of the fluid and therefore can be seen to add weight to the fluid. It is defined as

$$S_m = \rho g_i \quad (6)$$

Here g_i is the gravitational vector component along x_i . The modification of the energy equation to utilise potential temperature gradient can be achieved by the addition of a corrective heat source. From the divergence theorem

$$\int_V \nabla \cdot S_i dV = \int_A S_i n_i dA \quad (7)$$

where S_i is a vector. It can be seen that the corrective heat source must be

$$\int_A \frac{c_p \mu_t}{\sigma_T} \left(-\frac{g_i}{c_p} \right) n_i dA = \int_V \left(-\frac{c_p \mu_t}{\sigma_T} \right) \nabla \cdot \left(\frac{g_i}{c_p} \right) dV = \int_V S_u dV \quad (8)$$

And therefore the energy source term that must be added is

$$S_u = \nabla \cdot \left(-\frac{\mu_t}{\sigma_T} g_i \right) \quad (9)$$

Inspection of Eqs. (5) and (8) shows that the term g_i/c_p , the dry adiabatic lapse, will function by inducing heat transfer when the vertical temperature gradient $\partial T/\partial z$ is not equal to the dry adiabatic lapse rate. The heat transfer will therefore have a positive value for the unstable atmosphere when the vertical temperature gradient $\partial T/\partial z$ is greater than the adiabatic lapse rate and a negative value when the vertical temperature gradient $\partial T/\partial z$ is less than the adiabatic lapse rate, and the atmosphere is under stable stratification. Under neutral conditions there will be zero heat transfer and therefore adiabatic conditions. This is consistent with the assumptions in the derivation of the Monin–Obukhov similarity theory, where the heat flux through the surface layer is equal to the ground heat flux and the potential temperature gradient, and therefore the temperature profile, is dependent on this heat flux. The heat flux vertically is therefore determined by the deviation of the temperature gradient from the adiabatic lapse rate, with the positive or negative sign of the heat flux determined by the sign convention used.

2.2. Turbulence modelling

The RANS formulations for steady flow have been used in this study. The standard $k-\varepsilon$ turbulence model, first proposed by Launder and Spalding (1974), meets the requirement of accounting for shear and buoyancy produced turbulence, and has been widely deployed in ABL simulations; consequently there is a large availability of k and ε properties of the atmospheric boundary layer in meteorological data (Alinot and Masson, 2005). The $k-\varepsilon$ turbulence model achieves closure for the flow variables by introducing two additional transport equations for the turbulent kinetic energy (k) and turbulent kinetic energy dissipation rate (ε) (Alinot and Masson, 2005; Pontiggia et al., 2009), respectively:

$$\int_A \rho k u_i n_i dA = \int_A \frac{\mu_t}{\sigma_k} \frac{\partial k}{\partial x_i} n_i dA + \int_V [G_k + G_b - \rho \varepsilon] dV \quad (10)$$

$$\int_A \rho \varepsilon u_i n_i dA = \int_A \frac{\mu_t}{\sigma_\varepsilon} \frac{\partial \varepsilon}{\partial x_i} n_i dA + \int_V \left[C_{\varepsilon 1} \frac{\varepsilon}{k} (G_k) - C_{\varepsilon 2} \rho \frac{\varepsilon^2}{k} + S_\varepsilon \right] dV \quad (11)$$

$$G_k = \tau_{ij} \frac{\partial u_i}{\partial x_j} = -\rho \overline{u_i u_j} \frac{\partial u_i}{\partial x_j} = \frac{\partial u_i}{\partial x_j} \left(\mu_t \left(\frac{\partial u_i}{\partial x_j} + \frac{\partial u_j}{\partial x_i} \right) - \frac{2}{3} \rho k \delta_{ij} \right) \quad (12)$$

$$\mu_t = \rho C_\mu \frac{k^2}{\varepsilon} \quad (13)$$

Here the molecular dynamic viscosity μ has been ignored, as μ_t , the dynamic eddy viscosity, is much greater than μ . G_k is the turbulent kinetic energy production due to shear. G_b is the turbulent kinetic energy production source term due to buoyancy that must be added to the transport equation, and is given by

$$G_b = \beta g_i \frac{\mu_t}{\sigma_T} \left(\frac{\partial \theta}{\partial x_i} \right) = \beta g_i \frac{\mu_t}{\sigma_T} \left(\frac{\partial T}{\partial x_i} \frac{g_i}{c_p} \right) \quad (14)$$

where β is the thermal volumetric expansion coefficient. For an ideal gas the volumetric expansion coefficient is given by

$$\beta = -\frac{1}{\rho} \frac{\partial \rho}{\partial T} = \frac{1}{T} \quad (15)$$

Using the formulation of (Alinot and Masson, 2005) the source term that accounts for gravity effects in the ε -equation is

$$S_\varepsilon = C_{\varepsilon 1} \frac{\varepsilon}{k} (1 - C_{\varepsilon 3}) G_b \quad (16)$$

Notice again that the term g_i/c_p will function by inducing turbulence when the vertical temperature gradient $\partial T/\partial z$ is greater than the dry adiabatic lapse rate and the atmosphere is in unstable stratification, while it will remove turbulence when the atmosphere is stable and the vertical temperature gradient $\partial T/\partial z$ is less than the adiabatic lapse rate (Alinot and Masson, 2005). Under neutral conditions the turbulence source terms will be zero. Further, $C_{\varepsilon 1}$, $C_{\varepsilon 2}$, $C_{\varepsilon 3}$, σ_k , σ_ε , and C_μ are empirical constants originally determined by Launder and Spalding (1974), for neutral conditions, and their values are given in Table 1.

The same form of the source term for the buoyant production of turbulent kinetic energy can be added to other two-equation RANS models, such as the SST $k-\omega$ model, while it has been suggested that gravity effects only be reflected in the k -equation of the $k-\omega$ turbulence model (Peng and Davidson, 1999).

2.3. Description of the basic flow

In this study the flow is assumed to be represented by the conditions in the surface layer for flow over homogenous flat terrain with heat fluxes that lead to stable, neutral and unstable stratifications. The expressions describing the flow are based on the Monin–Obukhov similarity theory, in terms of the buoyancy or stability parameter

$$\zeta = z/L \quad (17)$$

where L is the Monin–Obukhov length and is defined as

$$L = \frac{u_*^2 T_0}{\kappa g \theta_*} \quad (18)$$

with θ_* , the scaling temperature, defined as

$$\theta_* = \frac{-\dot{q}_0}{\rho c_p u_*} \quad (19)$$

where u_* is the friction velocity, κ is the von Karman constant with an experimentally determined value of between 0.38 and 0.45 (Azad,

1993; Blackadar, 1997; Lumley, 1964), and T_0 is the temperature at ground level. From the definition it is clear that L may range from $-\infty$ to ∞ , with the extreme values occurring when the heat flux (\dot{q}_0) approaches zero from the positive (unstable) and the negative (stable) side (Arya, 2001a). The magnitude $|L|$ represents the height at which the magnitudes of mechanical and buoyant production of turbulence are equal (Arya, 2001a; Kröger, 2004).

The similarity prediction that follows from the Monin–Obukhov similarity hypothesis is that any mean flow or turbulence quantity in the surface layer, when normalised by an appropriate scaling parameter, must be a unique function of z/L only (Arya, 2001a; Arya, 2005). The dimensionless wind shear and potential temperature gradient can be expressed as:

$$\frac{\kappa z}{u_*} \left(\frac{\partial u}{\partial z} \right) = \varphi_m(\zeta) \quad (20)$$

$$\frac{\kappa z}{\theta_*} \left(\frac{\partial \theta}{\partial z} \right) = \varphi_h(\zeta) \quad (21)$$

where φ_m and φ_h are the universal similarity functions that relate the constant fluxes

$$\tau = \tau_0 = \rho u_*^2 \quad (22)$$

$$\dot{q} = \dot{q}_0 = -\rho c_p u_* \theta_* \quad (23)$$

to the mean gradients in the surface layer (Arya, 2001a). In addition, from exchange theory it can be seen that the dynamic turbulent viscosity μ_t is related to the similarity functions by

$$\mu_t = \frac{\rho \kappa u_* z}{\varphi_m(\zeta)} \quad (24)$$

The similarity functions must be determined empirically and the equations that will be employed in this study are those derived by Businger et al. (1971) and Dyer (1974)

$$\varphi_h = \varphi_m^2 = (1 - 16\zeta/L)^{-1/2}, \quad L < 0 \quad (25)$$

$$\varphi_h = \varphi_m = 1 + 5\zeta/L, \quad L > 0 \quad (26)$$

The vertical wind and temperature profiles can now be determined by integration and yields the following relations for wind velocity and potential temperature with respect to height:

$$u(z) = \left(\frac{u_*}{\kappa} \right) \left[\ln \left(\frac{z}{z_0} \right) - \psi_m \left(\frac{z}{L} \right) \right] \quad (27)$$

$$\theta(z) - \theta_0 = \left(\frac{\theta_*}{\kappa} \right) \left[\ln \left(\frac{z}{z_0} \right) - \psi_h \left(\frac{z}{L} \right) \right] \quad (28)$$

where θ_0 is the potential temperature at ground level (often equal to T_0), ψ_m and ψ_h are the integrated forms of the similarity functions and are given by

$$\psi_h = \psi_m = -5 \frac{z}{L}, \quad L > 0 \quad (29)$$

$$\psi_m = \ln \left[\left(\frac{1+x^2}{2} \right) \left(\frac{1+x}{2} \right)^2 \right] - 2 \tan^{-1} x + \frac{\pi}{2}, \quad L < 0 \quad (30)$$

$$\psi_h = 2 \ln \left(\frac{1+x^2}{2} \right), \quad L < 0 \quad (31)$$

where

$$x = (1 - 16\zeta/L)^{1/4} \quad (32)$$

It can be noted that the profiles will start to deviate from the log law with increasing values of z/L . Under stable conditions the profiles tend to become linear for large values of z/L and under

Table 1
Original $k-\omega$ model constants.

$C_{\varepsilon 1}$	$C_{\varepsilon 2}$	$C_{\varepsilon 3}$	σ_k	σ_ε	C_μ
1.44	1.92	0	1.0	1.3	0.09

unstable conditions ψ_m and ψ_h are positive so that the profiles of velocity and temperature will become more curvilinear. Based on the measurements of turbulent kinetic energy budget terms in the surface layer over flat terrain (Alinot and Masson, 2005), one can find

$$\varepsilon(z) = \frac{u_*^3}{\kappa z} \varphi_\varepsilon\left(\frac{z}{L}\right) \quad (33)$$

where

$$\varphi_\varepsilon\left(\frac{z}{L}\right) = \begin{cases} 1 - \frac{z}{L} & L < 0 \\ \varphi_m\left(\frac{z}{L}\right) - \frac{z}{L} & L > 0 \end{cases} \quad (34)$$

Solving the $k-\varepsilon$ equations yields the profile for k for thermally stratified atmospheric boundary layers (Alinot and Masson, 2005; Pontiggia et al., 2009)

$$k(z) = \sqrt{\frac{\mu_t \varepsilon}{\rho C_\mu}} = 5.48 u_*^2 \sqrt{\frac{\varphi_\varepsilon\left(\frac{z}{L}\right)}{\varphi_m\left(\frac{z}{L}\right)}} \quad (35)$$

where the constant 5.48 has been empirically determined for the neutral atmospheric boundary layer. To ensure that the profiles derived for velocity, temperature and turbulence properties from the Monin–Obukhov similarity theory are exact solutions to the $k-\varepsilon$ model, the values of the model constants C_μ , $C_{\varepsilon 1}$, and $C_{\varepsilon 3}$ must be changed (Alinot and Masson, 2005). From Eq. (35), by combining Eqs. (11) and (33) it is clear that the value of C_μ must be

$$C_\mu = 5.48^{-2} \quad (36)$$

while an expression for $C_{\varepsilon 1}$ can be obtained from the transport equation of ε , by introducing the empirical expressions of the Monin–Obukhov theory for neutral conditions (Alinot and Masson, 2005)

$$C_{\varepsilon 1} = C_{\varepsilon 2} - \frac{\kappa^2}{\sigma_\varepsilon \sqrt{C_\mu}} \quad (37)$$

Furthermore, many values of $C_{\varepsilon 3}$ have been suggested in the literature (Alinot and Masson, 2005; CD-adapco Inc., 2011; Kitada, 1987) and they range from -0.8 for unstable conditions to 2.15 for stable conditions. In this study, constant values of 3.4 under stable conditions and -4.4 for unstable conditions have been used for $C_{\varepsilon 3}$ (Alinot and Masson, 2005). It can be noted that Alinot and Masson (2002, 2005) have derived a function for $C_{\varepsilon 3}$, which is dependent on the stability parameter z/L . In this study, however, it was found that the solution was not significantly influenced by describing $C_{\varepsilon 3}$ with this function versus using the constant values. Further, the specific dissipation rate ω used in the $k-\omega$ turbulence model can be related to ε by

$$\omega = \varepsilon / C_\mu k \quad (38)$$

The full set of governing equations for continuity, momentum, energy and turbulent quantities could now be solved using the control volume based commercial CFD package STAR-CCM+. This was applied to the full scale unperturbed ABL flow in two-dimensions, the flow over a cosine shaped hill in a wind tunnel in three-dimensions, and the flow over an idealised two-dimensional transverse dune.

3. Full scale unperturbed ABL

3.1. Model set-up

The relevant parameters of the boundary layers that are to be simulated are given in Table 2. Stable, unstable and neutral

Table 2

Parameters describing the different stratified atmospheres.

ABL state	z_0 (m)	u_r (m/s)	z_r (m)	\dot{q}_0 (W/m ²)	T_0 (°C)	L (m)	u_* (m/s)	κ (/)	k_s (m)
Neutral	0.002	10	10	0	25	∞	0.481	0.41	0.015
Stable	0.002	10	10	−30	10	309.5	0.472	0.41	0.015
Unstable	0.002	10	10	100	40	−108.1	0.497	0.41	0.015

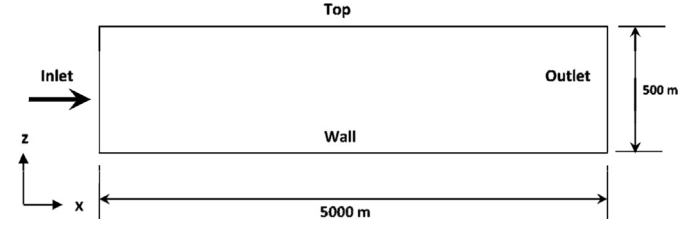


Fig. 1. Schematic of computational domain (not to scale).

atmospheres are to be modelled. The value specified for the aerodynamic roughness length corresponds to the “smooth” Davenport classification, applicable to featureless land surface without any noticeable obstacles and with negligible vegetation (Wieringa, 2001). Furthermore the equivalent sand-grain roughness height was calculated using

$$k_s = 7.5 z_0 \quad (39)$$

to ensure reasonable grid resolution close to the ground, due to the need to have the wall adjacent cell centroid (z_p) greater than k_s . All the profiles were chosen to have a reference velocity (u_r) of 10 m/s at a reference height (z_r) of 10 m, for easy comparison.

3.1.1. Computational domain and grid generation

The computational domain was a two-dimensional empty rectangle 500 m in height and 5000 m in length (Blocken et al., 2007b; Hargreaves and Wright, 2007; Parente et al., 2011b), and is shown schematically in Fig. 1. A three-dimensional STL (stereo lithography) surface file was created with dimensions of 500 m high, 5000 m long and 50 m wide, using CAD software. This surface file could be imported into STAR-CCM+ as a new fluid region, meshed and converted into a two-dimensional grid. The surface was meshed using hexahedral elements with a base size of 10 m. In addition, 25 orthogonal prismatic cells were added next to wall boundary, with a stretching ratio of 1.17 to a height of 10 m. It was furthermore decided to use a grid size that is similar to the grids used in practice, and therefore the mesh was further refined near the surface over the first 100 m in the vertical (z) direction to 50% of the base size.

The resulting two-dimensional mesh had 65,500 cells with an above ground cell centroid z_p of 0.0171 m, so that $z_p > k_s$. The resulting mesh was used for all the subsequent CFD calculations in this section. The grid had similar to finer resolution as grids used to investigate the ABL in other studies (Blocken et al., 2007b; Hargreaves and Wright, 2007; Parente et al., 2011b), and it was also observed that the findings were consistent for any grid of reasonable resolution.

3.1.2. Flow physics solution specification

The physics models used to specify the fluid were as follows: the fluid space was specified as two-dimensional and the time specification was steady. The material specified was air with the following properties: constant dynamic viscosity (μ) of 1.85508×10^{-5} Pa s; constant molecular weight (M) of 28.9664 kg/kmol; constant specific heat (c_p) of 1003.62 J/kg K; constant thermal conductivity (λ) of 0.0260305 W/m K; and a turbulent Prandtl

Table 3
Turbulence model constants for unperturbed ABL simulations.

Standard $k-\omega$	$C_{\varepsilon 1}$	$C_{\varepsilon 2}$	C_{μ}	σ_k	σ_{ε}			
	1.176	1.92	0.0333	1.0	1.3			
SST $k-\omega$	α_1	β_1	β_*	σ_{k1}	$\sigma_{\omega 1}$	β_2	σ_{k2}	$\sigma_{\omega 2}$
	0.31	0.075	0.09	0.85	0.5	0.0828	1.0	0.856

(σ_T) number of 1.0. The density was calculated through the ideal gas law. The segregated flow solver was chosen, which achieves pressure–velocity coupling through the SIMPLE algorithm, and solves the total energy equation through the segregated fluid temperature model, which uses temperature as the independent variable (CD-adapco Inc., 2011). Convection of momentum and energy was solved using the second-order upwind scheme. The turbulent viscous regime was chosen with turbulence modelled using the Reynolds-averaged Navier–Stokes (RANS) turbulence models.

Two different RANS models were investigated, namely the standard $k-\varepsilon$ model and the SST $k-\omega$ model. In both cases the high z^+ wall treatment was used which represents the classic wall function approach (note that z^+ is referred to as y^+ in the fluid mechanics literature, but is renamed for consistency with the coordinate system used in this study), where the wall shear stress and turbulence parameters are all derived from equilibrium turbulent boundary layer theory, and requires that the near wall cell lies within the logarithmic region of the boundary layer (CD-adapco Inc., 2011). It thus requires that z^+ be between the values of 30 and 500. The z_p (0.0171 m) for the computational mesh used in this analysis yielded a z^+ value of about 450 along the length of the bottom wall, thereby satisfying both the requirement of $z_p > k_s$ and $z^+ < 500$ (Blocken et al., 2007b). The turbulence model constants used for the simulations are given in Table 3.

A reference pressure of 101,325 Pa was used, which is applied by default at the point [0, 0] in the fluid domain (CD-adapco Inc., 2011). The flow was initialised using the inlet boundary conditions for velocity, temperature, and turbulence quantities defined below, as well as zero pressure. The solution was run until the normalised residuals of continuity, momentum, energy and turbulence had converged, while additionally the velocity and temperature at various points along the fetch were monitored to ensure that they too converged to a constant value.

3.1.3. Boundary conditions

The velocity inlet boundary was the z line located upstream of the fluid domain. The static temperature, velocity components (u_x equal to $u(z)$ with zero u_y and u_z) and turbulence properties were specified here using the “Table (x, y, z)” method, where the properties along the vertical height of the domain were calculated in Microsoft Excel (2010) and exported in comma delimited (CSV) format, from where they could be imported into STAR-CCM+. The velocity and temperature profiles given by Eqs. (27)–(32) were used to specify the inlet velocity and temperature. The vertical distributions of k and ε given by Eqs. (33) and (35) were used to specify the inlet turbulence parameters and Eq. (38) was used to specify the specific dissipation rate (ω). The pressure is internally calculated from the continuity equation and the density is calculated by the code from the ideal gas law. In addition, the velocity, temperature and turbulence quantities at the outlet of the domain, 5000 m downstream, could be used as a new set of inlet conditions to a new simulation. This was done to effectively extend the fetch to 10,000 m. The profiles were found to have stabilised sufficiently after the first 5000 m, although strictly speaking this approach can only be valid if the profiles do not change along the fetch.

Table 4
Flow values specified at top boundary for unperturbed ABL.

ABL state	$[u_x, u_y, u_z]$ (m/s)	T (K)	k (J/kg)	ε (J/kg s)	ω (s^{-1})
Neutral	[14.593, 0, 0]	293.11	1.2699	0.000544	0.0129
Stable	[23.629, 0, 0]	280.65	1.1089	0.003838	0.1039
Unstable	[12.622, 0, 0]	304.09	5.5069	0.003368	0.0184

The outlet boundary is the vertical z line downstream of the fluid domain that was specified as a “flow-split outlet” with a split ratio of one. This type of boundary allows the pressure and temperature profiles to develop from the inlet conditions, rather than having to impose a pressure and temperature here that could over-constrain the solution.

The top boundary is the x line at the top of the fluid domain where the undisturbed flow conditions were prescribed. This includes the velocity components, the temperature and the turbulence quantities. The values for these quantities for the different thermal stability conditions are given in Table 4.

The bottom fluid boundary that was specified as a wall had the high z^+ wall treatment imposed. The shear stress specification was selected as no-slip and the thermal specification was achieved by specifying the ground temperature found in Table 2. The wall surface specification was defined as rough with a roughness constant equal to k_s in Table 2.

3.2. Results and discussion

The streamwise homogeneity of the velocity and turbulence profiles under neutral conditions for the $k-\varepsilon$ turbulence model are shown in Fig. 2, along with the temperature, density and pressure profiles. It is clear that the velocity profile (Fig. 2(a)) is well maintained throughout a substantial downstream distance. A slight acceleration of the flow is observed close to the ground, which is consistent with the observation of previous studies (Blocken et al., 2007b; Hargreaves and Wright, 2007). The turbulence profiles too are well maintained, with the turbulent kinetic energy (Fig. 2(b)) shown to decay in the downstream direction, more so after the first 1000 m. The turbulent kinetic energy dissipation rate (Fig. 2(c)) also decays in the downstream direction, but this is likely due to the decay observed in the turbulent kinetic energy. The greatest errors in the profiles are seen close to ground, where energy is being removed by shearing.

The temperature, density and pressure (relative to the reference pressure) profiles are shown in Fig. 2(d), (e) and (f) for neutral conditions modelled with $k-\varepsilon$ turbulence, respectively. Also shown in the plots are the theoretical values expected for the neutral atmosphere, with density calculated from the ideal gas law. These profiles calculated by the code for pressure and density correspond well with the theoretical values, with the temperature being the adiabatic lapse rate and specified at the inlet. The temperature profile furthermore is maintained well and thereby too the density. It is seen that the pressure is virtually invariant along the entire length of the domain. This is a good result as horizontal homogeneity requires that the pressure must simply balance the weight of the fluid and lead to density variation, while the flow is driven by the shear induced at the top boundary by

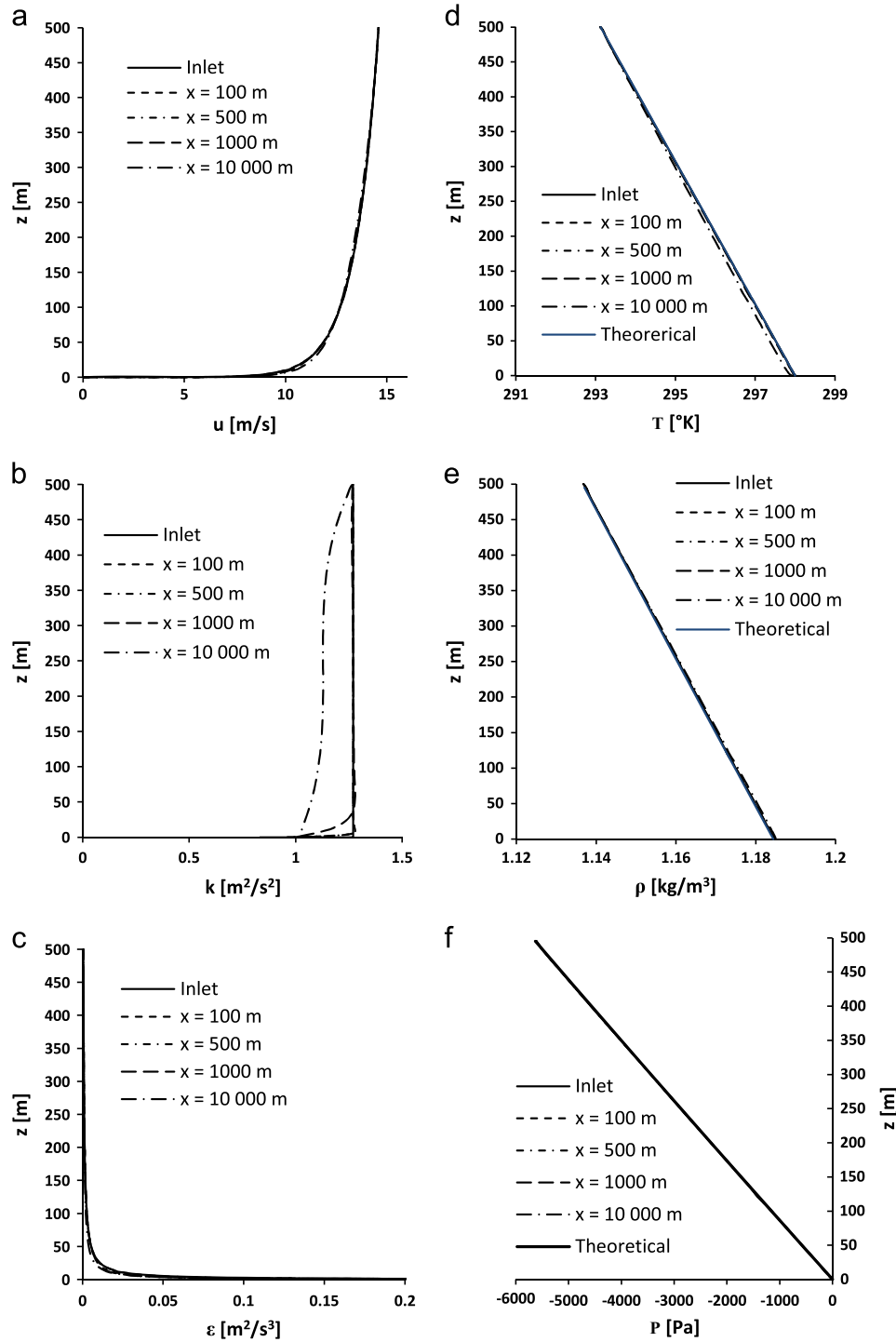


Fig. 2. Neutral CFD $k-\omega$ model results illustrating streamwise gradients for (a) wind speed u , (b) turbulent kinetic energy k , (c) turbulent dissipation rate ϵ , (d) temperature T , (e) density ρ , and (f) pressure P . Theoretical values for the neutral atmosphere also shown.

specifying a horizontal velocity there. This velocity has the effect of feeding momentum into the flow and driving it along. There is consequently no need for a large pressure gradient to develop between the inlet and the outlet of the domain, and the pressure profile is therefore completely dominated by the hydrostatic effect.

Inspection of Fig. 2(b) reveals that the k -value is under predicted at the first cell centroid above the wall. The subsequent decay of the profile extends from this point up in the vertical direction. This phenomenon will be shown to occur consistently for the subsequent simulations of the stable and unstable atmosphere too, and suggests an issue with the wall function approach.

The results of the homogeneity error in the flow properties for the simulation of the stable atmosphere using the $k-\epsilon$ turbulence model are shown in Fig. 3. We again observe a slight acceleration of the flow velocity (Fig. 3(a)) in the lower part of the domain and decay in the turbulent kinetic energy profile (Fig. 3(b)). Similar to the k -profile error observed for the neutral conditions, we see that the turbulent kinetic energy is under predicted in the first node above the wall. The temperature (Fig. 3(d)), density (Fig. 3(e)) and pressure (Fig. 3(f)) profiles, however, are well maintained. The results for the analysis of the homogeneity errors in the flow parameters for the unstable atmosphere are shown in Fig. 4 for the

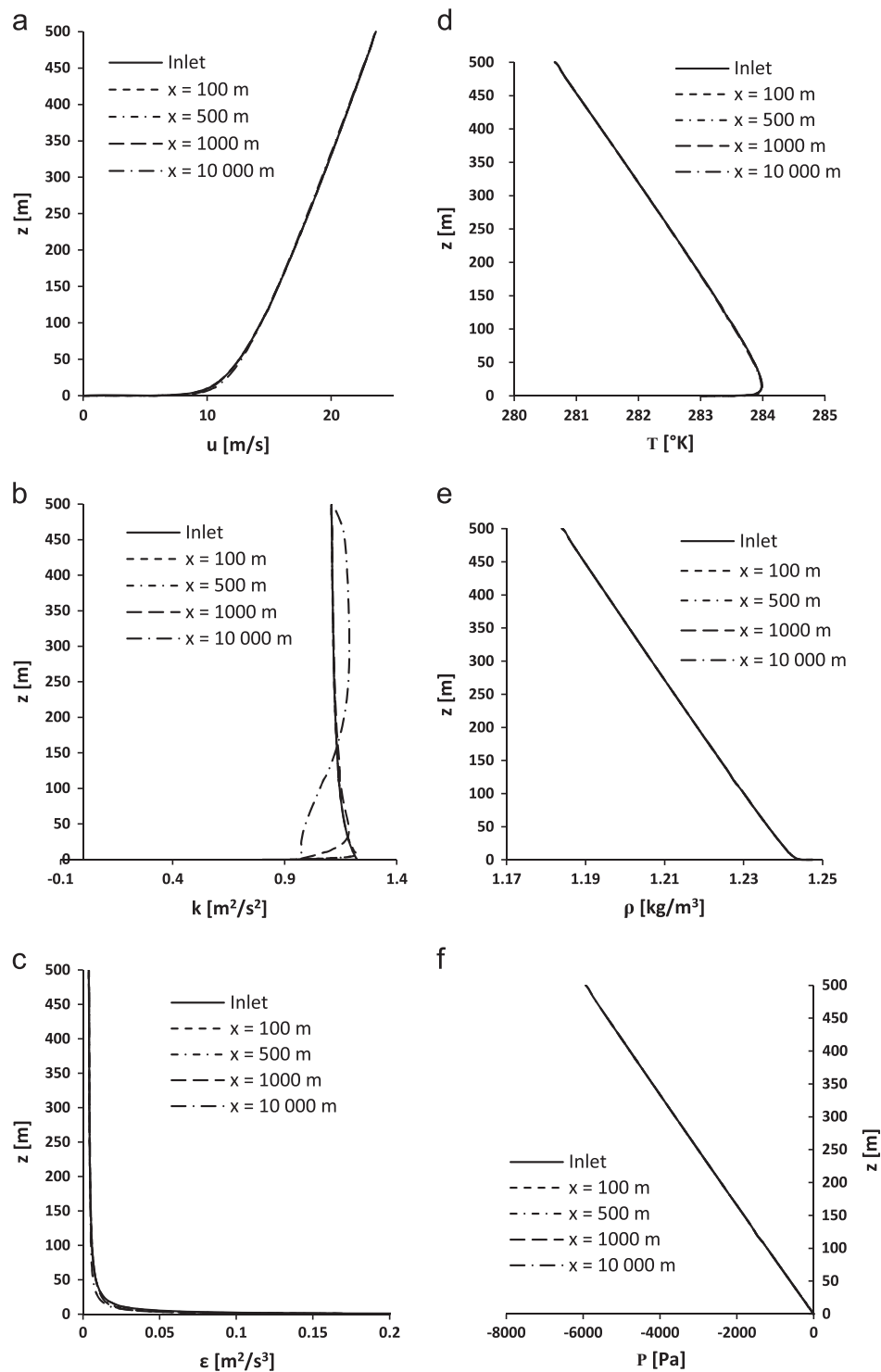


Fig. 3. Stable CFD $k-\omega$ model results illustrating streamwise gradients for (a) wind speed u , (b) turbulent kinetic energy k , (c) turbulent dissipation rate ε , (d) temperature T , (e) density ρ , and (f) pressure P .

$k-\varepsilon$ turbulence model. The results for the unstable atmosphere are qualitatively similar to the results achieved for the neutral and stable atmospheres.

A comparison of the homogeneity error at a height of 10 m, relative to the inlet conditions, is shown in Fig. 5 for neutral (a), stable (b) and unstable (c) conditions. The error made by the SST $k-\omega$ turbulence model is also shown here. It illustrates clearly the higher errors made by the $k-\omega$ turbulence model, but shows that the error starts to stabilise in the downstream direction after

approximately the first 1000 m. It can also be seen that the temperature profile is almost equally well maintained by both turbulence models. The homogeneity errors for the neutral, stable and unstable atmospheres were consistently similar, and therefore reveal that these profiles were equally well maintained along the fetch of the domain. In all cases good convergence of the solution was found and therefore minimal numerical instability was encountered. The fact that the pressure was found to vary very little along the length of the fluid domain for all the thermal

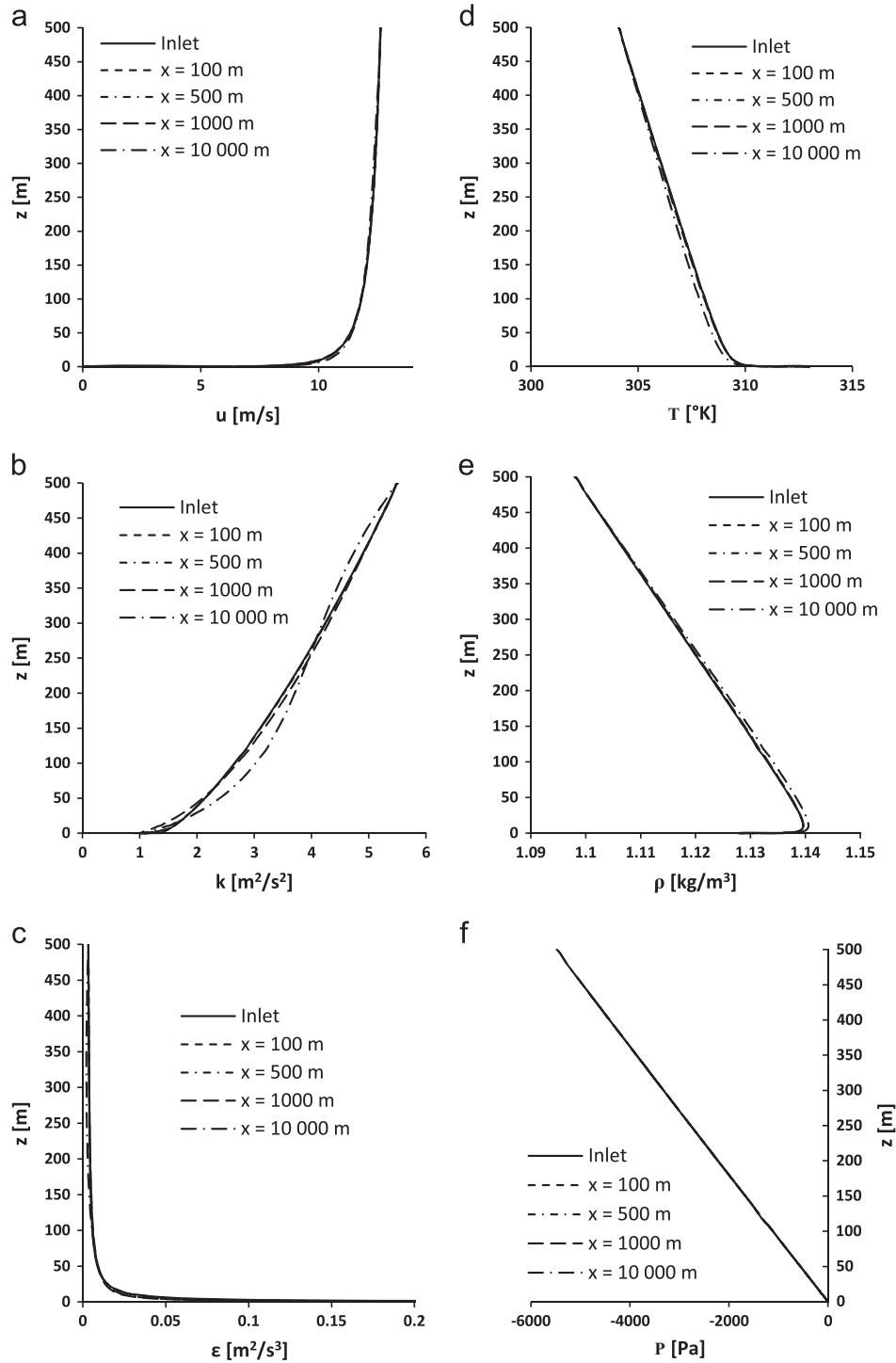


Fig. 4. Unstable CFD $k-\omega$ model results illustrating streamwise gradients for (a) wind speed u , (b) turbulent kinetic energy k , (c) turbulent dissipation rate ε , (d) temperature T , (e) density ρ , and (f) pressure P .

stratifications is consistent with the assumptions of the horizontally homogenous ABL, with the flow instead being driven by the velocity specified at the top boundary, and therefore by shear.

The maintenance of the velocity and temperature profiles for all the thermal stratifications were found to be particularly good, with less than 10% error at a height of 10 m, the point in the domain where the some of the largest inhomogeneity was observed. Other studies have found that the temperature profiles cannot be maintained without inducing numerical instability

(Huser et al., 1997; Meissner et al., 2009; Pontiggia et al., 2009), something which has been attained in this study.

The inconsistencies in the k -profiles and the value of the turbulent kinetic energy calculated at the first grid point above the wall points to the wall function being inconsistent with the turbulence profiles. This inconsistency is likely to be the reason for the streamwise gradients induced in the flow domain. This is a consistent problem in the CFD simulation of the ABL and has been encountered by many researchers (Blocken et al., 2007a; Franke et al., 2011; Hargreaves and Wright, 2007; Parente et al., 2011b;

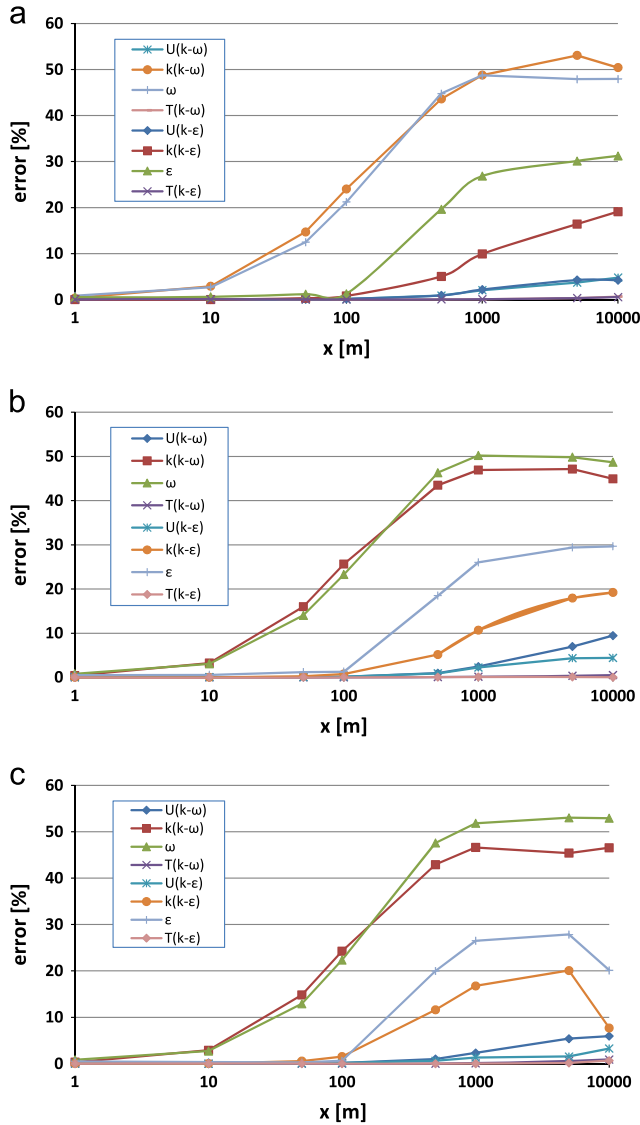


Fig. 5. Relative change of the flow parameters for the $k-\omega$ and $k-\epsilon$ turbulence models relative to the inlet for (a) neutral, (b) stable, and (c) unstable conditions.

Yang et al., 2008). Remedial measures have been suggested which includes the reformulation of the wall function from a k_s based treatment to a z_0 based treatment (Blocken et al., 2007b; Parente et al., 2011a).

The manipulation of the code in commercial CFD packages like FLUENT (Fluent 2006) or STAR-CCM+ to make these kinds of modifications are not straightforward and are much more easily implemented in open-source software like OpenFOAM (Balogh et al., 2012). The reason is that commercial codes do not allow access to the source code, and for this reason the current wall functions provided for use in the code have to suffice.

The effect of the homogeneity error can, however, be minimised by keeping the domain as short as possible. It should further be noted that profiles with higher surface roughness, not presented here, proved more difficult to maintain, as the resolution close to the ground was limited by the roughness height and the turbulent kinetic energy produced was also higher. The higher turbulent kinetic energy leads to increased momentum exchange between the fluid layers which lead to an increase in the acceleration of the velocity close to the ground (Blocken et al., 2007b). Furthermore, the reduction of the wind speed leads to a reduction in the shear produced turbulence, and leads to a more dominant

role of the buoyancy produced turbulence. The buoyancy effects therefore start to become significant at lower speeds and increase the observed homogeneity error for profiles of lower wind speed, particularly under unstable conditions, with the solution also taking much longer to converge.

It can be noted that the assumption in surface layer modelling is constant fluxes of momentum and heat with height, equal to the surface shear stress and heat flux. It would be expected that the accuracy of the CFD model will improve if the shear stress and heat flux could be specified at the top of the domain, thus forcing a constant flux of heat and momentum through the boundary layer that is consistent with the theory and the inlet profiles. This sort of boundary treatment in STAR-CCM+ unfortunately is also not straightforward, but it is a recommended treatment for future investigations where boundaries can easily be customised, such as in OpenFOAM.

In general then, it is advisable that for every CFD simulation involving ABL flow, the effects of horizontal inhomogeneity first be assessed by performing a simulation in an empty computational domain. This is especially true if the ABL is modelled under the effects of thermal stratification, as for certain combinations of flow variables and surface parameters the error induced in the streamwise direction can be large. It can be concluded that while the $k-\epsilon$ turbulence model proved to be better equipped to maintain the flow properties along the fetch of the domain, it is known to be less accurate in separated regions, an area where the SST $k-\omega$ turbulence model is known to perform well (Yang et al., 2008). It only needs to be shown, thus, that the SST $k-\omega$ turbulence model can adequately maintain the flow properties of the thermal stratified ABL, which has been demonstrated here.

4. Separated flow over a cosine shaped hill

4.1. Model set-up

The CFD models, modified to account for gravity effects, could now be tested against experimental data. These measurements were obtained in the thermally stratified wind tunnel of the University of Tokyo, using three-dimensional laser Doppler anemometry (Takahashi et al., 2005). The model is an axisymmetric cosine shaped hill of scale 1/1000, with the height h defined in terms of the radius r by

$$h(r) = \begin{cases} H \left[1 + \cos \left(\frac{2\pi r}{R_b} \right) \right] & \text{if } r < R_b \\ 0 & \text{otherwise} \end{cases} \quad (40)$$

where R_b is the radius of the hill base and has a value of 0.42 m, with the maximum height of the hill H given as 0.2 m.

The boundary conditions for the velocity and turbulent kinetic energy were derived for the results presented by Takahashi et al. (2005) for the incident flow in the wind tunnel, and the results of the flow field around the hill model for the mean streamwise velocity and the turbulent kinetic energy were used for comparison to the CFD results.

The turbulence models tested included the standard $k-\epsilon$ turbulence model and the SST $k-\omega$ turbulence model modified for gravity effects. In addition two other steady RANS models were used namely: the realisable $k-\epsilon$ turbulence model (which was modified in a similar way as the standard $k-\epsilon$ turbulence model) and the Spalart-Allmaras turbulence model (which was run with its default values). An implicit unsteady detached eddy simulation (DES) model, derived from the SST $k-\omega$ turbulence model, was also employed.

The conditions for the neutral or unheated wind tunnel were used. The parameters derived from the incident (model position in wind tunnel without the model) profile of velocity are shown in

Table 5

Parameters derived from neutral wind tunnel incident flow.

z_0 (m)	u_H (m/s)	H (m)	δ (m)	T_0 (°C)	u_δ (m/s)	L (m)	u_s (m/s)	κ (/)	k_s (m)
0.000676	1.174	0.2	0.7	17	1.42	∞	0.0845	0.41	0.00507

Table 5. The reference velocity (u_H) used was the velocity at the height of the model in the empty wind tunnel, and the reference height was the model height (H). The height of the boundary layer (δ) was found to be about 0.7 m with a velocity here of 1.42 m/s, which was the maximum velocity the profile attained. The mean flow velocity (u_m) at the model position in the wind tunnel without the model was found to be 1.0572 m/s. Additionally the turbulent intensities of the incident velocity profile were provided as a root mean square value of the velocity fluctuations in the x -, y - and z -directions, from which of turbulent kinetic energy could be calculated.

The flow measurements were also carried out for stable and unstable boundary layers in the thermally stratified wind tunnel. It was, however, found that the temperature profiles enforced on the incident flow could not be maintained by the CFD code. The temperature gradients were found to be too large for the model to handle and considerable heat conduction occurred resulting in a severe distortion of the inlet profiles. It should be noted that the CFD equations were modified to account for the temperature and velocity gradients typically occurring in the atmosphere and not the severe gradients imposed by the wind tunnel.

4.1.1. Computational domain and grid generation

The working section of the wind tunnel is 2.2 m wide and 1.8 m high. As the profiles for the incident flow on the hill were available it was decided to place the inlet of the domain at least $8H$ upstream of the hill (Franke et al., 2011) and therefore the model was placed 2 m downstream from the inlet. It is further recommended that when using an outflow boundary it must be placed at least $15H$ from the obstruction (Franke et al., 2011), a downstream length of 6 m was chosen to resemble the overall size of the wind tunnel and to allow for flow recovery. To save on computational requirements only half of the model and wind tunnel was simulated, with the addition of a symmetry boundary along the central lengthwise axis of the domain.

A three-dimensional STL (stereo lithography) surface file was created using CAD software and imported into STAR-CCM+. The surface was meshed using hexahedral elements with a base size of 40 mm. In addition, three orthogonal prismatic cells were added next to wall and hill boundary, with a stretching ratio of 1.05 to a height of 33.3 mm. The mesh around the hill was further refined in all directions to 25% of the base size.

The resulting three-dimensional mesh had 602,796 hexahedral cells with a z_p of 0.0053 m over the wind tunnel floor and over the hill surface (so that $z_p > k_s$). A grid sensitivity analysis was carried out to determine the solution error associated with the discretisation, using the procedure of Celik et al. (2008). The investigation was performed using two additional grids with a refinement ratio of 1.3, based on the representative grid size. This resulted in a coarser and a finer mesh with 328,031 and 1,363,693 cells, respectively. The medium mesh thus specified proved to provide acceptable discretisation error, based on the re-attachment length, velocity and turbulent kinetic energy in the wake of the hill.

4.1.2. Flow physics solution specification

The wind tunnel simulation boundary conditions and physics models were chosen to reflect as closely as possible the simulations

carried out for the unperturbed ABL. The physics models used to specify the steady RANS simulations were as follows: the fluid space was specified as three-dimensional and the time specification was steady. The material specified was again air and the density was calculated through the ideal gas law. The segregated flow solver was chosen, and the total energy equation was solved through the segregated fluid temperature model (CD-adapco Inc., 2011). Convection of momentum and energy was achieved using the second-order upwind scheme. The turbulent viscous regime was chosen and the Reynolds-averaged Navier–Stokes (RANS) turbulence models were specified.

A reference pressure of 101,325 Pa was again used. The flow was initialised using the inlet boundary conditions for velocity, temperature, and turbulence quantities defined below, as well as zero pressure. The solution was run until the normalised residuals of continuity, momentum, energy and turbulence had converged, while additionally the velocity and temperature at various points along the fetch were monitored to ensure that they too converged to a constant value.

The implicit unsteady solver was used for the DES turbulence model, which is derived from the SST $k-\omega$ turbulence model, and the initial conditions were the converged flow solutions achieved using the steady state SST $k-\omega$ turbulence model. Further the same physics models were used as for the steady RANS simulations. A time step of 0.005 s was specified for a maximum physical time of 5 s. The maximum inner iterations were set to 15 iterations per time step as this was found to be sufficient for the normalised residuals to decrease by at least three orders of magnitude. For a cell length of 0.01 m and a velocity of 1.5 m/s, the time step gave a Courant–Friedrichs–Lewy number of 0.75.

The Spalart–Allmaras turbulence model is a one-equation RANS model and therefore the turbulent production due to buoyancy cannot be specified as it can for the two-equation models. Under the neutral wind tunnel conditions there should, however, not be any buoyant turbulence production. The turbulence model constants for each turbulence model used are shown in Table 6.

4.1.3. Boundary conditions

As the CFD had to contend with separated flow, it was considered important to get as high a possible grid resolution close to the wind tunnel floor and the hill. Therefore the mesh was generated so that z_p was just greater than the value specified for the roughness height k_s . This yielded a z^+ value of between 10 and 50 over the floor and the hill. This situation therefore required the use of a blended wall function and can be specified in STAR-CCM+ by the all z^+ wall treatment, which is a hybrid approach between the low- z^+ and high z^+ wall functions (CD-adapco Inc., 2011). In the case of the $k-\omega$ turbulence models the Wolfstein two-layer formulation was used. The value of the roughness height was specified on the floor of the wind tunnel, which was modelled as a rough wall with the no-slip shear stress specification, as well as

Table 6

Turbulence model constants for hill simulation.

Standard $k-\omega$	C_{e1}	C_{e2}	C_μ	σ_k	σ_ω				
	1.176	1.92	0.0333	1.0	1.3				
Realisable $k-\omega$	C_{e1}	C_{e2}	C_μ	σ_k	σ_ω				
	1.152	1.90	0.0333	1.0	1.2				
SST $k-\omega$	α_1	β_1	β_*	σ_{k1}	$\sigma_{\omega1}$	β_2	σ_{k2}	$\sigma_{\omega2}$	
	0.31	0.075	0.09	0.85	0.5	0.0828	1.0	0.856	
Spalart–Allmaras	C_{b1}	C_{b2}	C_{prod}	C_{v1}	C_{w2}	C_{w3}	κ	σ_v	
	0.1355	0.622	2.0	7.1	0.3	2.0	0.41	2/3	
SST $k-\omega$ DES	$C_{DES\omega}$	$C_{DES\kappa}$	$C_{DES\tau}$						
	0.78	0.61	1.0						

the hill which received the same boundary treatment. Additionally the floor and hill had the temperature T_0 from Table 4 specified. The side wall and ceiling were selected as smooth walls with adiabatic thermal specification and with the no-slip condition also applied. The symmetry boundary was used on the symmetry plane of the wind tunnel and model, while the downstream flow outlet was specified as a “flow-split outlet” with a split ratio of one.

For all the simulations the adiabatic lapse rate temperature was specified at the inlet using a user “field function” relative to the floor temperature, although the change in temperature with height was virtually negligible. The x -direction velocity in each case was specified through a user “field function” by Eq. (27) (with zero u_y and u_z), using the values given in Table 4. The $k-\varepsilon$ and $k-\omega$ turbulence models had the turbulent kinetic energy that was measured in the incident flow specified at the inlet. The Spalart–Allmaras turbulence model required the definition of turbulence intensity I and turbulent length scale l through

$$I = \frac{\left(\frac{2}{3}k\right)^{1/2}}{u_m} \quad (41)$$

$$l = \frac{\kappa z}{1 + \kappa z/l_\infty} \quad (42)$$

where u_m is the mean flow velocity and l_∞ is the asymptotic mixing length (Griffiths and Middleton, 2010) given by

$$l_\infty = \kappa \delta \quad (43)$$

Here δ is the boundary layer height given in Table 4.

4.1.4. Comparison of measurements with CFD results

The CFD and experimental results could be compared using hit rates as a quality assessment metric. This quantity indicates the fraction of the N measurement locations where the CFD results are within a 25% interval of the experimental data (Britter and Schatzmann, 2007). Normalised values are used, with the reference wind speed and hill height used for normalisation.

The distributions of x -velocity and turbulent kinetic energy along the central plane of the hill (on the symmetry plane) were normalised with the reference velocity u_H and compared with vertical distributions of the wind tunnel data at values of x/H of 0, 1.125, 2.25, 3, 4, 5.5 and 7, where 0 corresponds to the centre point of the hill, and the other points are all in the wake. In all cases the measured data corresponds to the published data of Takahashi et al. (2005).

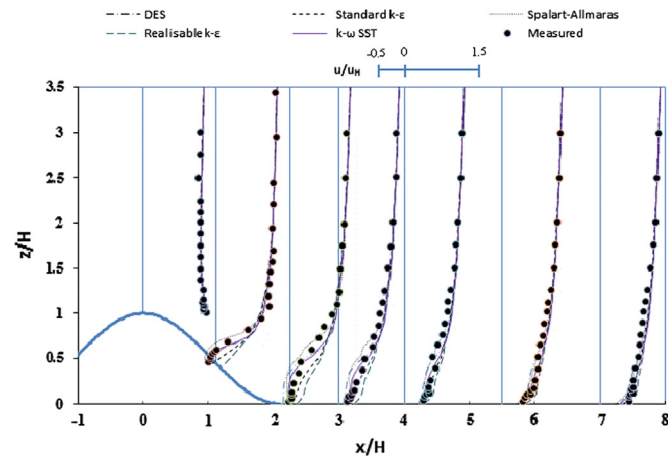


Fig. 6. Comparison of the horizontal velocity results against measurement.

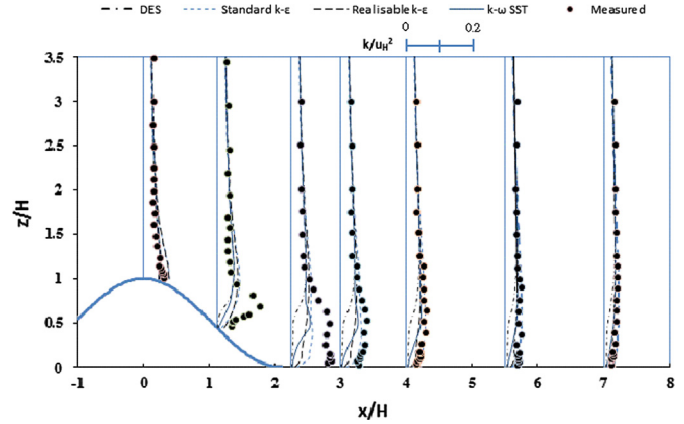


Fig. 7. Comparison of the turbulent kinetic energy results against measurement.

4.2. Results and discussion

The results of the comparison of the different turbulence models for flow over the cosine shaped hill against measured data are shown in Fig. 6 for the streamwise velocity and in Fig. 7 for the turbulent kinetic energy. The results for the DES are the time averaged results of the simulation.

The velocity results reveal that all the turbulence models correspond well with the measured data of the velocity distributions at the top of the hill, and then again after about four hill heights downstream. It is in the recirculating flow zone and immediately after it where the turbulence models tended to give different results. It was found that the realisable $k-\omega$ turbulence model predicted no separation in the wake of the hill, with the x -direction velocity never becoming negative. The standard $k-\omega$ turbulence model yielded some separation but still under predicted the size and extent of the separation bubble, suggesting faster flow recovery. On the other hand, the Spalart–Allmaras turbulence model over predicted the influence of the adverse pressure gradient with larger separation bubble prediction than that shown by the measured data. It was the SST $k-\omega$ turbulence model that gave the best prediction of the separated region directly in the wake of the hill, and also showed the best correspondence with the measured data for the size of the separation bubble.

The time averaged DES data showed a similar trend as the steady state SST $k-\omega$ turbulence model, but tended to over predict the separated zone downstream of the hill compared to the steady state model. There may be several reasons for this, which include that perhaps the 5 s that was simulated was not sufficient to capture the full range of transient behaviour in the wake of the hill. It should be noted that the sampling time for one wind tunnel measurement was 45 s with 2000 samples for one measurement (Takahashi et al., 2005). It is therefore suggested that the DES be simulated for a longer time span. It was, however, not feasible for this particular study as the computational time required for the DES simulation was considerably more than for the steady state RANS turbulence models.

It was nevertheless found that the steady state RANS models were capable of fairly accurate prediction of the separated region, particularly the SST $k-\omega$ turbulence model, which is consistent with the findings of Yang et al. (2008). It is furthermore achieved with considerably less computational requirements than for unsteady simulations, making high turnover of different simulations possible. Unless one was interested in transient effects like vortex shedding, which was observed in the unsteady DES simulation, it is suggested that steady state turbulence models can suffice.

The results of the hit rates analysis are shown in Table 7. It is seen that the percentage scores of the SST $k-\omega$ turbulence model and the standard $k-\omega$ turbulence model were the highest for

velocity, suggesting that they most closely corresponded to the measurements. The SST $k-\omega$ turbulence model, however, was better at predicting the flow in the immediate wake of the hill. For this reason the SST $k-\omega$ turbulence model was used in the simulation of the flow over the idealised transverse dune immersed in the thermally stratified ABL, in the next section.

It was the turbulent kinetic energy distributions that the turbulence models had the hardest time reproducing. This was found to be particularly true in the immediate wake regions of the flow, where the measurements showed a much more pronounced peak close to the ground than predicted by any of the turbulence models. These results are similar to those found by Balogh et al. (2012) using FLUENT and OpenFOAM. They found that the results could be marginally improved, particularly for the prediction of the turbulent kinetic energy distributions, by modifying the wall treatments to be consistent with the velocity and turbulence inlet profiles in OpenFOAM (Balogh et al., 2012). This kind of wall treatment, however, is not available to users of STAR-CCM+, and its implementation is made difficult as access to the source code is unavailable.

5. Thermally stratified flow over an idealised transverse dune

5.1. Model set-up

It was now possible to investigate the flow field around an idealised two-dimensional transverse dune immersed in a thermally stratified ABL. The SST $k-\omega$ turbulence model, modified for gravity effects, was used to model the flow field. The dune geometry was a scaled up version of the dune modelled by Liu et al. (2011), and is described in Table 8.

The parameters describing the thermally stratified ABL are given in Table 9. These values are consistent with profiles measured by the authors in the Namib Desert interdune area, with the results not presented here.

Table 7
Hit rate values for simulations over cosine hill.

Cases	Streamwise velocity (%)	Turbulent kinetic energy (%)
Spalart–Allmaras	69.1	/
$k-\omega$ SST	71.9	36.9
Realisable $k-\omega$	67.6	44.1
Standard $k-\omega$	71.9	31.5
DES	69.1	30.6

Table 8
Dune geometry parameters.

Parameter	Value
Dune height (h)	10 m
Windward base length	56.71 m
Leeward base length	17.32 m
Windward slope angle	10°
Leeward slope angle	30°

Table 9
Parameters describing the different stratified atmospheres for dune simulation.

ABL state	z_0 (m)	u_h (m/s)	h (m)	\dot{q}_0 (W/m ²)	T_0 (°C)	L (m)	u_s (m/s)	κ (/)	k_s (m)
Neutral	0.04	6.9	10	0	25	∞	0.499	0.40	0.04
Stable	0.04	6.9	10	–30	10	348.0	0.487	0.40	0.04
Unstable	0.04	6.9	10	400	40	–38.5	0.555	0.40	0.04

5.1.1. Computational domain and grid generation

The minimum upstream distance of the inlet from an obstruction should be at least 8 h (Franke et al., 2011). The inlet was therefore placed 150 m from the crest of the dune. It is further recommended that when using an outflow boundary it must be placed at least 15 h from the obstruction (Franke et al., 2011), and therefore this boundary was placed 300 m from the dune crest to ensure sufficient flow recovery. Again, a three-dimensional STL surface file was created using CAD software and imported into STAR-CCM+. The surface was meshed using hexahedral elements with a base size of 5 m. In addition, 24 orthogonal prismatic cells were added next to the wall and dune boundary, with a stretching ratio of 1.09 to a height of 5 m. The mesh around the dune was further refined in all directions to 25% of the base size. The resulting three-dimensional mesh was then converted into a two-dimensional mesh.

The resulting two-dimensional mesh had 17,328 cells with a z_p of 0.041 m on the ground and the dune, so that $z_p > k_s$. A grid sensitivity analysis was carried out to using the procedure of Celik et al. (2008). The investigation was performed using two additional grids with a refinement ratio of 1.3, based on the representative grid size. This resulted in a coarser and a finer mesh with 6717 and 38,755 cells, respectively. The medium mesh thus specified proved to provide acceptable discretisation error, based on the re-attachment length, velocity and turbulent kinetic energy in the wake of the dune.

5.1.2. Flow physics solution specification

The physics models used were as follows: the fluid space was specified as two-dimensional and the time specification was steady. The material specified was air with the density calculated through the ideal gas law. The segregated flow solver was chosen, and the total energy equation was solved. Convection of momentum and energy was solved using the second-order upwind scheme. The turbulent viscous regime was chosen and the Reynolds-averaged Navier–Stokes (RANS) turbulence models were specified. The SST $k-\omega$ turbulence model was selected.

A reference pressure of 101,325 Pa was used. The flow was initialised using the inlet boundary conditions for velocity, temperature, and turbulence quantities defined below, as well as zero pressure. Furthermore, the models had the momentum and energy source terms accounting for gravity effects specified, as well as the turbulence sources due to gravity. The turbulence model constants are shown in Table 10. Solution convergence was adjudged in the same way as previously stated.

5.1.3. Boundary conditions

The CFD once again had to contend with separated flow and good grid resolution close to the dune surface and the ground was therefore required. The mesh was generated so that z_p was just

Table 10
Turbulence model constants for dune simulations.

SST $k-\omega$	α_1	β_1	β_*	σ_{k1}	$\sigma_{\omega 1}$	β_2	σ_{k2}	$\sigma_{\omega 2}$
	0.31	0.075	0.09	0.85	0.5	0.0828	1.0	0.856

Table 11
Flow values specified at top boundary.

ABL state	$[u_x, u_y, u_z]$ (m/s)	T (K)	k (J/kg)	ω (s^{-1})
Neutral	[11.343, 0, 0]	294.65	1.369	0.0196
Stable	[17.181, 0, 0]	281.31	1.187	0.1050
Unstable	[9.987, 0, 0]	301.11	9.987	0.0370

greater than the value specified for the roughness height k_s . This treatment yielded an average z^+ value of roughly 500 for the ground and the dune. The high z^+ wall treatment was therefore implemented. The value of the roughness height was specified on the ground, which was modelled as a rough wall with the no-slip shear stress specification, as well as the dune which received the same boundary treatment. Additionally the ground and the dune had the temperature T_0 from Table 9 specified.

The inlet boundary upstream of the fluid domain had the static temperature, velocity components and turbulence properties specified. The vertical distributions of k and ω given by Eqs. (35) and (38) were used to specify the inlet turbulence parameters. The pressure is internally calculated from the continuity equation and the density is calculated by the code from the ideal gas law.

The top boundary is where the undisturbed flow conditions were prescribed. The values for these quantities for the different thermal stability conditions are given in Table 11. The downstream flow outlet had a split ratio of one.

5.2. Results and discussion

The isovel contour plots of the streamwise velocity for the different thermally stratified atmospheres are shown in Fig. 8. The model is seen to predict flow deceleration immediately upwind of the dune, followed by windward slope acceleration with a maximum velocity at the crest, and then negative flow in the separation bubble. Another observation is the convergence in the faster upper isovels of the flow fields, which corresponds to a zone of “jet” of accelerated, overshoot flow which extends from the crest above the flow separation bubble (Parsons et al., 2004a). These results are consistent with those of other dune flow studies (Liu et al., 2011; Livingstone et al., 2007; Parsons et al., 2004a; Parsons et al., 2004b). It is clear that this overshoot flow is less pronounced in the stable flow case (Fig. 8(b)) and more pronounced in the unstable case (Fig. 8(c)). This is consistent with our understanding of the behaviour of flow under different thermal stratifications. One expects that flow that is vertically displaced by an obstacle will be decelerated by buoyancy in the stable atmosphere, while buoyancy forces will accelerate the flow displaced vertically in an unstable atmosphere. This results in greater acceleration of the flow above the dune crest in the unstable case, and less flow acceleration in the stable case.

These observations can also partly be explained by the higher turbulent viscosities present in the unstable atmosphere, where higher turbulent viscosity leads to increased mixing in the flow and therefore faster flow recovery in the wake. These results are qualitatively similar to the wind tunnel observations of thermally stratified flow over a hill reported by Takahashi et al. (2005). This effect too is reflected in the calculation of re-attachment length, where the shear stress on the wall is zero, for the different thermally stratified atmospheres, shown in Table 12. Flow re-attachment takes longer in the stable case, followed by the neutral case, with the re-attachment happening considerably earlier for the unstable atmosphere. These results for re-attachment length are also consistent with previous flow simulations for idealised transverse dunes under neutral conditions (Liu et al., 2011; Parsons et al., 2004a; Parsons et al., 2004b).

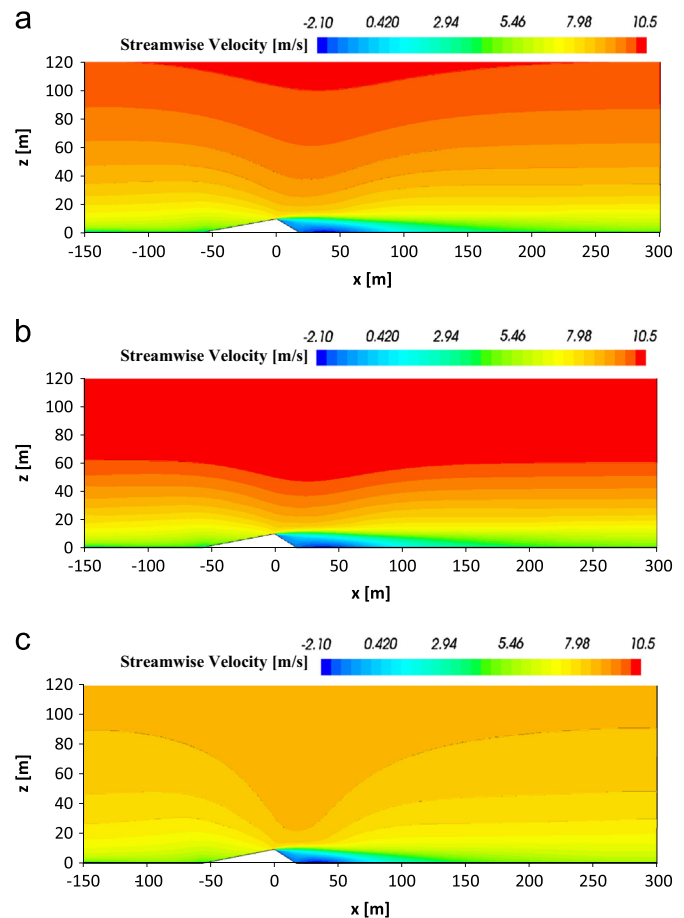


Fig. 8. Contour plots of horizontal (streamwise) velocity for (a) neutral conditions, (b) stable conditions, and (c) unstable conditions.

Table 12
Flow re-attachment lengths for different stability conditions.

ABL state	(x/h)
Neutral	8.0625
Stable	8.1875
Unstable	7.0625

Fig. 9 shows the vertical velocity field for the different thermally stratified atmospheres. A zone of positive upward flow exists on the windward slope and reaches a maximum at the crest, which is related to the upward forcing effect of the dune. Small pockets of upward moving air are also seen on the leeward slope as the recirculating zone drives the air up the dune face. A zone of strongly downward moving air exists in the lee and extends above the flow separation zone from the base of the leeward slope to beyond the flow re-attachment point. This too is consistent with previous observations (Liu et al., 2011; Livingstone et al., 2007; Parsons et al., 2004a; Parsons et al., 2004b). As expected for the stable atmosphere (Fig. 9(b)) the upward and downward vertical velocities are less pronounced than in the other two cases. A greater upward velocity is seen on the windward side and a greater negative velocity is seen on the leeward side in the unstable case (Fig. 9(c)).

This is once again explained by the physics of the thermally stratified atmosphere where a vertically displaced air parcel will be decelerated in the stable atmosphere and accelerated upwards

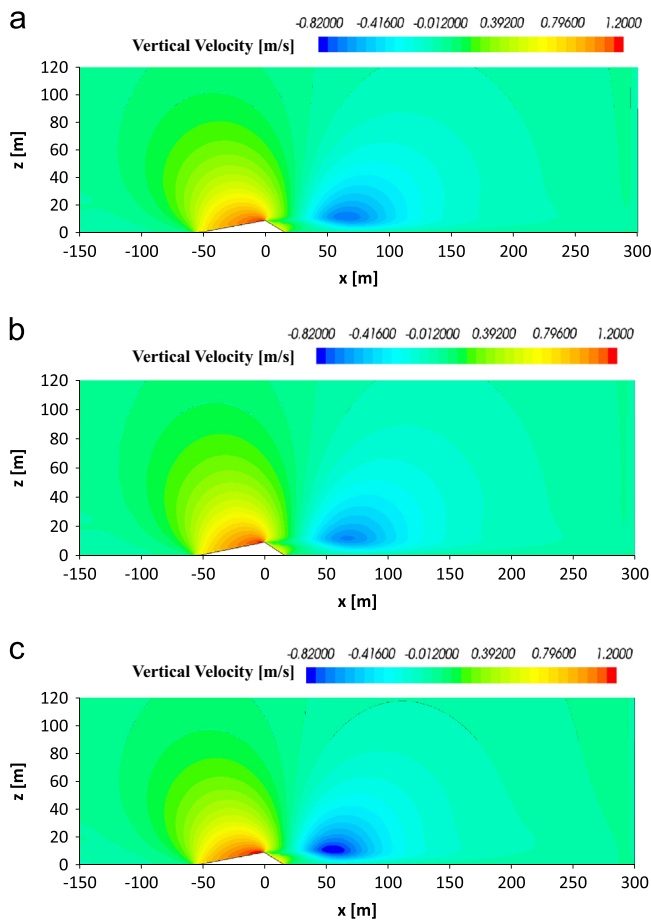


Fig. 9. Contour plots of vertical velocity for (a) neutral conditions, (b) stable conditions, and (c) unstable conditions.

or downwards in the unstable atmosphere. This larger negative vertical velocity also helps to explain the lower re-attachment length seen for the unstable case, while the stable atmosphere's smaller negative velocity contributes to the longer re-attachment length. A larger zone of upward moving air is also seen on the lee side of the unstable case compared to the neutral and stable cases.

It should therefore be clear that the thermal stratification of the atmosphere can have a significant effect of the flow field over a sand dune. This has implications for the prediction of sand and seed transport which influences the dynamics of desert geomorphology, and it can also have an effect on the overall dune geometry. The CFD study of these kinds of structures cannot therefore be limited to the neutral atmosphere as the thermally stratified atmosphere is prevalent in desert areas, with stable conditions predominating at night and unstable condition predominating during the day.

The non-dimensional results of the horizontal (streamwise) velocity obtained for the neutral atmosphere, additionally using the standard $k-\epsilon$ turbulence model, are shown in Fig. 10, along with the non-dimensional measurements from the wind tunnel study of Liu et al. (2011). The flow field of the wind tunnel study was found to be Reynolds number independent, and similarity existed for the wind speed profiles, allowing the non-dimensional results to be compared. Reasonable agreement is found between the experimental data and the numerical results. The flow acceleration on the upwind slope (–2.8 h, Fig. 10(c)), the pronounced velocity gradient on the dune crest (0 h, Fig. 10(d)) and the flow separation and recirculation in the dune wake (1.7 h, Fig. 10(e)) were reproduced by the CFD simulations. Generally the airflow field of the wind tunnel study is well represented by the CFD

models but with noticeable disagreement in the near wall zones at some of the measurement locations. This was also seen by Liu et al. (2011) who attributed it to the limitation of the measuring system which cannot resolve the high-speed gradients in the near-surface zone. It was further observed, as expected, that the SST $k-\omega$ turbulence model (hit rate 90.5%) generally performed better than the standard $k-\epsilon$ turbulence model (hit rate 88.6%), which showed greater acceleration at the dune crest and faster downstream flow recovery than suggested by the measured data.

It was found that the standard $k-\epsilon$ turbulence model consistently predicted slightly higher turbulent viscosities than the SST $k-\omega$ turbulence model. This was particularly true in the wake region, where it was seen that the $k-\epsilon$ turbulence model over predicts the flow recovery, attributed to the greater mixing effect brought about by the higher turbulent viscosity. Both turbulence models predicted larger negative velocities in the separation bubble (1.7 h, Fig. 10(e)) than those that were measured. This can be ascribed to either the limitation of the measuring system, or the three-dimensional effects present in the wind tunnel that are unaccounted for by the CFD, where Liu et al. (2011) found lateral dispersion of the separation bubble along the leeward face for the three-dimensional case.

It has therefore been shown that the flow field over a dune is potentially greatly influenced by the thermal stability of the atmosphere and this is surely true for other structures immersed in the thermally stratified ABL. With an increasing emphasis being placed on renewable energy, accurate wind resource prediction models are required. The ABL becomes increasingly more influenced by the thermal stability condition with increasing height, which can lead to discrepancies in the wind speed predictions which could result in less than expected power outputs from wind turbines, particularly in areas where unstable conditions predominate. This has been shown by Alinot and Masson (2002). The prediction of thermal stability has implications on pollution dispersion models as well, where the stable atmosphere could lead to the build-up of particulates in the lower atmosphere. The accurate CFD modelling of the thermally stratified atmosphere is therefore very important in wind studies, as it has been confirmed here that the assumption of neutral conditions could lead to an incomplete picture of the flow conditions that influence any particular case of interest. For airflow over desert sand dunes the influence of the thermal stability condition of the atmosphere has been found to play a significant role.

6. Conclusions

A procedure for simulating the thermally stratified ABL using CFD was described in this study. In each case the numerical solution was found to be stable with good levels of solution convergence. The simulation demonstrated the capability of maintaining the temperature, velocity and turbulence profiles along an extensive downstream flow distance, therefore displaying high levels of horizontal homogeneity, a precondition for accurate CFD wind model predictions. The CFD model further demonstrated the capability of accounting for buoyancy and gravity effects, by allowing for the full variation of density, temperature and pressure.

In each case the hydrostatic pressure, and the density variation that it brings about, developed in the flow field by the addition of the fluid weight into the momentum equation, thus also introducing buoyancy forces. It was further found that gravity effects could be introduced into several two-equation RANS turbulence models, which displayed the advantage of lower computational requirement, leading to higher simulation turnover than for other turbulence models like DES. The turbulence models thus modified

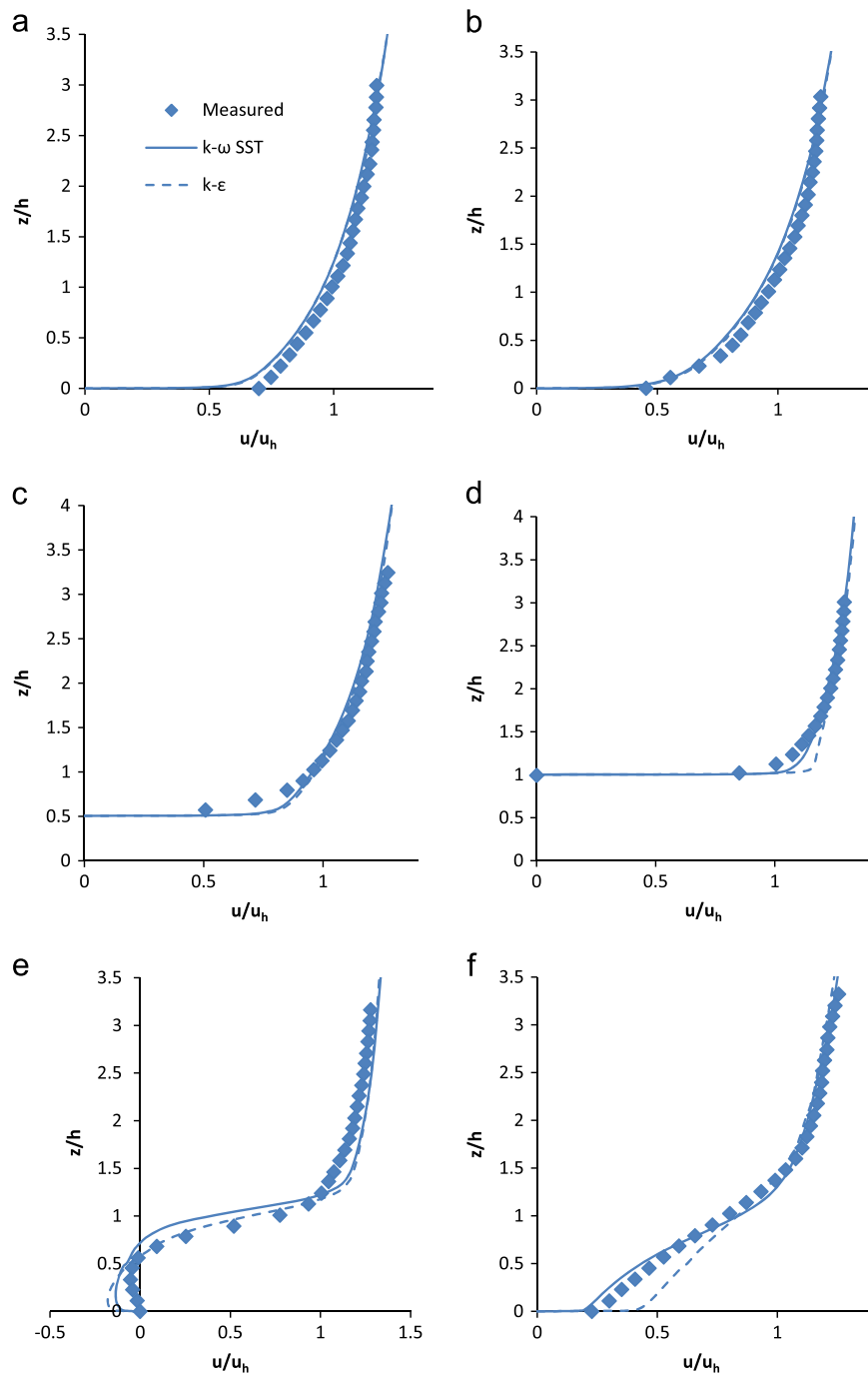


Fig. 10. Standard $k-\epsilon$ and SST $k-\omega$ turbulence model streamwise velocity for neutral conditions versus measurement at six positions relative to dune crest: 8 h (a), –5.6 h (b), –2.8 h (c) 0 h (d) 1.7 h (e) and 10 h (f).

displayed decent performance in simulating separated regions in the flow field, with the SST $k-\omega$ turbulence model providing results that best aligned to measured experimental data.

Furthermore, it was shown that the thermal stability of the atmosphere can have significant effects on the flow field over a sand dune. It was found that the flow recovery was enhanced and re-attachment occurred earlier in unstable conditions. Flow recovery and re-attachment took longer in stable conditions. It was also found that flow acceleration over the crest of the dune was greater under unstable conditions and that the effect of the dune on the flow higher up in the atmosphere was felt at much higher distances. Under stable conditions, however, the influence on the flow higher up in the atmosphere was much less than for unstable

or neutral conditions. Vertical velocities were also enhanced for a dune immersed in the unstable ABL and reduced for stable conditions. The accurate CFD modelling of the thermally stratified atmosphere is therefore very important in wind studies, as it has been confirmed here that the assumption of neutral conditions could lead to an incomplete picture of the flow conditions that influence any particular case of interest

Acknowledgements

The authors wish to acknowledge the assistance provided through the use of its facilities of the Gobabeb Research and Training

Centre, Namib Desert, Namibia, and gratefully acknowledge the funding received for this research under the Food Security Program of the Stellenbosch University Hope initiative.

References

- Alinot, C., Masson, C. 2002. Aerodynamic simulations of wind turbines operating in atmospheric boundary layer with various thermal stratifications. In: ASME Conference Proceedings 2002, pp. 206–215.
- Alinot, C., Masson, C., 2005. $k-\epsilon$ Model for the atmospheric boundary layer under various thermal stratifications. *Journal of Solar Energy Engineering* 127, 438–443.
- Arya, S.P., 2001a. Thermally stratified surface layer. In: Holton, H. (Ed.), *International Geophysics*. Academic Press, New York, pp. 213–241 (Chapter 11).
- Arya, S.P., 2001b. Air temperature and humidity in the PBL. In: Holton, H. (Ed.), *International Geophysics*. Academic Press, New York, pp. 62–88 (Chapter 5).
- Arya, S.P., 2005. Micrometeorology and atmospheric boundary layer. *Pure and Applied Geophysics* 162, 1721–1745.
- Azad, R.S., 1993. *The Atmospheric Boundary Layer for Engineers*. Kluwer, Dordrecht.
- Balogh, M., Parente, A., Benocci, C., 2012. RANS simulation of ABL flow over complex terrains applying an enhanced $k-\epsilon$ model and wall function formulation: implementation and comparison for fluent and OpenFOAM. *Journal of Wind Engineering and Industrial Aerodynamics* 104, 360–368.
- Blackadar, A.K., 1997. *Turbulence and Diffusion in the Atmosphere*. Springer-Verlag, Berlin.
- Blocken, B., Carmeliet, J., Stathopoulos, T., 2007a. CFD evaluation of wind speed conditions in passages between parallel buildings—effect of wall-function roughness modifications for the atmospheric boundary layer flow. *Journal of Wind Engineering and Industrial Aerodynamics* 95, 941–962.
- Blocken, B., Stathopoulos, T., Carmeliet, J., 2007b. CFD simulation of the atmospheric boundary layer: wall function problems. *Atmospheric Environment* 41, 238–252.
- Britter, R., Schatzmann, M., 2007. *Model Evaluation Guidance and Protocol Document*. COST Office, Brussels.
- Businger, J.A., Wyngaard, J., Izumi, Y., Bradley, E., 1971. Flux–profile relationships in the atmospheric surface layer. *Journal of the Atmospheric Sciences* 28, 181–189.
- CD-adapco Inc. 2011. *STAR-CCM+ Version 6.02.007 User Guide*. CD-adapco Inc., New York.
- Celik, I.B., Ghia, U., Roache, P.J., 2008. Procedure for estimation and reporting of uncertainty due to discretization in CFD applications. *Journal of fluids (Engineering-Transactions) of the ASME*, 130.
- Dyer, A., 1974. A review of flux–profile relationships. *Boundary-Layer Meteorology* 7, 363–372.
- Franke, J., Hellsten, A., Schlunzen, K.H., Carissimo, B., 2011. The COST 732 Best Practice Guideline for CFD simulation of flows in the urban environment: a summary. *International Journal of Environment and Pollution* 44, 419–427.
- Garratt, J., 1994. Review: the atmospheric boundary layer. *Earth-Science Reviews* 37, 89–134.
- Griffiths, A., Middleton, J., 2010. Simulations of separated flow over two-dimensional hills. *Journal of Wind Engineering and Industrial Aerodynamics* 98, 155–160.
- Hargreaves, D., Wright, N., 2007. On the use of the $k-\epsilon$ model in commercial CFD software to model the neutral atmospheric boundary layer. *Journal of Wind Engineering and Industrial Aerodynamics* 95, 355–369.
- Huser, A., Nilsen, P.J., Skåtun, H., 1997. Application of $k-\epsilon$ model to the stable ABL: pollution in complex terrain. *Journal of Wind Engineering and Industrial Aerodynamics* 67–68, 425–436.
- Kim, S.E., Boysan, F., 1999. Application of CFD to environmental flows. *Journal of Wind Engineering and Industrial Aerodynamics* 81, 145–158.
- Kitada, T., 1987. Turbulence structure of sea breeze front and its implication in air pollution transport—application of $k-\epsilon$ turbulence model. *Boundary-Layer Meteorology* 41, 217–239.
- Kröger, D.G., 2004. *Air-cooled heat exchangers and cooling towers: thermal-flow performance evaluation and design*. Penwell Corporation.
- Launder, B.E., Spalding, D., 1974. *The numerical computation of turbulent flows*. *Computer Methods in Applied Mechanics and Engineering* 3, 269–289.
- Liu, B., Qu, J., Zhang, W., Qian, G., 2011. Numerical simulation of wind flow over transverse and pyramid dunes. *Journal of Wind Engineering and Industrial Aerodynamics* 99, 879–888.
- Livingstone, I., Wiggs, G.F.S., Weaver, C.M., 2007. Geomorphology of desert sand dunes: a review of recent progress. *Earth-Science Reviews* 80, 239–257.
- Lumley, J.S.P., 1964. *The structure of atmospheric turbulence*. Wiley-Interscience, New York.
- Meissner, C., Gravdahl, A.R., Steensen, B., 2009. Including thermal effects in CFD simulations 2012.
- Parente, A., Gorié, C., van Beeck, J., Benocci, C., 2011a. A comprehensive modelling approach for the neutral atmospheric boundary layer: consistent inflow conditions, wall function and turbulence model. *Boundary-Layer Meteorology* 140, 411–428.
- Parente, A., Gorié, C., van Beeck, J., Benocci, C., 2011b. Improved $k-\epsilon$ model and wall function formulation for the RANS simulation of ABL flows. *Journal of Wind Engineering and Industrial Aerodynamics* 99, 267–278.
- Parsons, D.R., Walker, I.J., Wiggs, G.F.S., 2004a. Numerical modelling of flow structures over idealized transverse aeolian dunes of varying geometry. *Geomorphology* 59, 149–164.
- Parsons, D.R., Wiggs, G.F.S., Walker, I.J., Ferguson, R.I., Garvey, B.G., 2004b. Numerical modelling of airflow over an idealised transverse dune. *Environmental Modelling & Software* 19, 153–162.
- Peng, S.H., Davidson, L., 1999. Computation of turbulent buoyant flows in enclosures with low-Reynolds-number $k-\omega$ models. *International Journal of Heat and Fluid Flow* 20, 172–184.
- Pontiggia, M., Derudi, M., Busini, V., Rota, R., 2009. Hazardous gas dispersion: a CFD model accounting for atmospheric stability classes. *Journal of Hazardous Materials* 171, 739–747.
- Rodi, W., 1997. Comparison of LES and RANS calculations of the flow around bluff bodies. *Journal of Wind Engineering and Industrial Aerodynamics* 69, 55–75.
- Takahashi, T., Kato, S., Murakami, S., Ooka, R., Fassy Yassin, M., Kono, R., 2005. Wind tunnel tests of effects of atmospheric stability on turbulent flow over a three-dimensional hill. *Journal of Wind Engineering and Industrial Aerodynamics* 93, 155–169.
- Wieringa, J., 2001. New revision of Davenport roughness classification. In: *Proceedings of the 3EACWE*, Eindhoven, The Netherlands, pp. 285–292.
- Wiggs, G.F.S., Livingstone, I., Warren, A., 1996. The role of streamline curvature in sand dune dynamics: evidence from field and wind tunnel measurements. *Geomorphology* 17, 29–46.
- Yang, W., Quan, Y., Jin, X., Tamura, Y., Gu, M., 2008. Influences of equilibrium atmosphere boundary layer and turbulence parameter on wind loads of low-rise buildings. *Journal of Wind Engineering and Industrial Aerodynamics* 96, 2080–2092.